Volume 1 | Number 1 | Jan 2013 | Pages 1–100

Journal of
Materials Chemistry A

Materials for energy and sustainability
www.rsc.org/materialsA

Li⁺

ROYAL SOCIETY
OF CHEMISTRY

ROYAL SOCIETY
OF CHEMISTRY

www.rsc.org/materialsA

NiO nanorod arrays anchored Ni foam as binder-free anode for high-rate lithium ion batteries†

Wanfeng Yang,[a] Guanhua Cheng,[a] Chaoqun Dong,[a] Qingguo Bai,[a] Xiaoting Chen,[a] Zhangquan Peng, *[b] Zhonghua Zhang*[a]

[a]Key Laboratory for Liquid-Solid Structural Evolution and Processing of Materials (Ministry of Education), School of Materials Science and Engineering, Shandong University, Jingshi Road 17923, Jinan, 250061, P.R. China

[b]State Key Laboratory of Electroanalytical Chemistry, Changchun Institute of Applied Chemistry, Chinese Academy of Sciences, Changchun, Jilin 130022, China

*Corresponding author. Email: zh_zhang@sdu.edu.cn (Z. Zhang), zqpeng@ciac.ac.cn (Z.Peng)

Tel/Fax: +86-531-88396978.

†Electronic Supplementary Information (ESI) available: [SEM images and Capacity-Cycle number Curves]

Here we report the preparation of 3D binder-free NiO nanorod-anchored Ni foam electrodes, and their application as anode materials for rechargeable lithium-ion batteries. By anodization followed with thermal annealing, blooming flower-like NiO arrays were anchored to Ni foam, and were characterized via X-ray diffraction (XRD), scanning electron microscopy (SEM), transmission electron microscopy (TEM) and N$_2$ adsorption/desorption experiment. Electrochemical properties were evaluated by cyclic voltammetry (CV) and galvanostatic cycling. Cycling performance shows that after 70 cycles the NiO nanorod-anchored Ni foam electrode can still deliver a stable reversible capacity

up to 705.5 mAh g^{-1} and 548.1 mAh g^{-1} with high coulombic efficiency ($\geq$ 98%) at a constant current density of 1 A g^{-1} and 2 A g^{-1}, respectively. Superior performance of the NiO electrode can be attributed to its favorable morphology and the excellent electrical contact between NiO and the current collector of Ni foam. The present strategy can be extended to fabricate other self-supported transition metal oxide nanostructures for high-performance lithium-ion batteries.

Introduction

Rechargeable lithium-ion batteries (LIBs) are regarded as an ideal power source for portable electronics, and also a potential candidate for hybrid electric vehicles (HEVs) and electric vehicles (EVs). However, for the application of the latter, i.e. electric transportation, energy materials superior to those used in the current generation LIBs need to be identified.[1-5] Therefore, numerous efforts have been devoted to develop new electrode materials with high energy density, power density and excellent cycling performance.[6,7] Compared with conventional carbon-based anode materials, transition metal oxides (TMOs, where TM = Fe, Co, Ni, Cu, etc.) have been identified as promising anode materials, due to their higher theoretical capacities which are based on a conversion reaction: $TMO + 2Li^+ + 2e^- \leftrightarrow Li_2O + TM$, different from the classical insertion/de-insertion or Li-alloying processes.[8] Among them, NiO has attracted great attention owing to its high capacity, low-cost, environmental friendliness and natural abundance. The theoretic capacity of NiO is

718 mAh g^{-1}, almost double that of graphite (372 mAh g^{-1} for Li$_x$C$_6$).[9] Furthermore, the density of NiO is 6.67 g cm^{-3}, resulting in 5.8 times over graphite in volumetric energy density.[10] Unfortunately, its practical application in LIBs is still hindered by its poor cycling stability and rate capability because of the intrinsic low conductivity and drastic volume variation in the discharge-charge process.[11] The current strategies to overcome these obstacles mainly address two issues: to construct nanostructures,[12-17] and to fabricate new composites with electrically conductive materials.[10,18-28] On the other hand, the widely used organic binder (polyvinylidene fluoride, PVDF) in conventional electrodes also tends to cause seriously poor stability and irreversible capacity losses. Because it is found to swell easily in common electrolyte with ethylene carbonate (EC)/dimethyl carbonate (DMC) solvent.[29] Recently, Co-doped NiO nanoflake array electrodes fabricated by chemical bath deposition delivered a capacity of 589.5 mA h g^{-1} after 50 cycles at 100 mA g^{-1}, but the capacity retention was only 66.8%, showing serious capacity decay.[13] NiO nanosheet/graphene composites were synthesized by hydrothermal reaction combined with heat treatment, which just ran 50 cycles at an extremely low current density of 50 mA g^{-1}.[22] The electrochemical performance was inevitably impeded by adding inactive and insulate polymeric binders. Alternatively, active materials directly anchored to the current collector have been fabricated through diverse approaches such as plasma assisted oxidation,[30] hydrothermal synthesis and electrodeposition.[20,31] Nevertheless, the practical application of this composite with such an attractive architecture was hampered due to some drawbacks of these

methods like complicated processing technology, requirement of special equipment and long-time consumption. Therefore, it is still a challenge to develop a facile strategy to fabricate binder-free electrodes with high reversible capacity and excellent rate capability for advanced LIBs.

Herein, a facile efficient in-situ anodization followed by thermal annealing was employed to fabricate 3D binder-free NiO nanorod-anchored Ni foam electrodes with excellent cycling stability and rate capability for high power LIBs. The as-prepared NiO nanorod-anchored Ni foam electrode achieves a stable reversible capacity up to 705.5 mAh g^{-1} and 548.1 mAh g^{-1} after 70 cycles with high coulombic efficiency at a constant current density of 1 A g^{-1} and 2 A g^{-1}, respectively, which could be attributed to its favorable morphology and the excellent electrical contact between NiO and Ni substrate.

Experimental section

Fabrication of NiO nanorod-anchored Ni foam electrode

NiO nanorod-anchored Ni foam electrode was fabricated by anodization using a homemade two-electrode system, followed by annealing treatment in a resistance furnace. Ni foams with thickness of 0.5 mm were used as the source of metal precursor for the growth of NiO nanorods. Anodization process was carried out at the temperature of -5 $^{\circ}$C, with a pure Ni foil (10 mm*3 mm*0.1 mm, 99.9 wt.%) as cathode and a Ni foam (20 mm*20 mm*0.5 mm, 99.9 wt.%) as anode. A 0.3 M oxalic acid (AR) aqueous solution was used as the electrolyte and the anodized voltage was

kept constant at 50 V for 10 min. The as-anodized Ni foams were rinsed with deionized water for several times to remove the residual acid, and then dried at $100\,^{\circ}C$ for 1 h in vacuum. The thermal decomposition of the resulting samples was conducted by annealing at $400\,^{\circ}C$ in air for 40 min, and the NiO nanorod-anchored Ni foam electrode was obtained after the annealing procedure. For a comparison, the directly annealed Ni foam was prepared under the same conditions except anodization. The loading amount of active NiO on the Ni foam was determined according to a calculation principle which was mainly based on the mass changes during the course of thermal annealing. The as-prepared nickel foams ($2*2$ cm^2) were dried and weighted. After annealing at $400\,^{\circ}C$, we weighted the samples again and calculated the weight change of each sample. The loading amount of NiO on the Ni foam was determined according to the following reaction： $NiC_2O_4 \cdot 2H_2O + O_2 \rightarrow NiO + 2H_2O + 2CO_2$ for the NiO nanorod-anchored Ni foam electrode and $2Ni + O_2 \rightarrow 2NiO$ for the directly annealed Ni foam electrode.

Morphological and structural characterization

X-ray diffraction (XRD) measurements of the as-prepared NiO nanorod-anchored Ni foam were performed on an X-ray diffractometer (XRD, Rigaku D/max-rB) with Cu Kα radiation. The morphology and microstructure of the as-prepared samples were characterized by a scanning electron microscope (SEM, LEO 1530 VP), together with a transmission electron microscope (TEM, FEI Tecnai G2). Additionally, selected-area electron diffraction (SAED) pattern was also obtained to document the

crystalline nature of the as-obtained samples. The fast Fourior transform (FFT) pattern was obtained from the corresponding high resolution TEM (HRTEM) image using software named Gatan Digital Micrograph. The TEM specimens were prepared using a Gatan ion mill at 5 kV. N_2 adsorption-desorption isotherms of the samples were carried out at 77 K by a Gold APP V-Sorb 2800P surface area and porosity analyzer. Brunauer-Emmett-Teller (BET) method was used to calculate the specific surface area. The pore size distribution was measured from the adsorption branch of isotherm using the corrected form of Kelvin equation by the Barrett-Joyner-Halenda (BJH) method.

Electrochemical characterization

The NiO nanorod-anchored Ni foam and the directly annealed Ni foam were punched into disks with a diameter of 12 mm as the working electrode, and a pure lithium metal foil served as both the counter electrode and reference electrode. The electrolyte solution was 1 M $LiPF_6$ dissolved in a mixture of EC/DMC with a volume ratio of 1:1 and the separator was polypropylene (PP) film (Celgard 2325). The CR2032-type coin cells were assembled in an argon-filled glove box with oxygen and moisture levels below 1 ppm. The cells were aged overnight before measurement. Cyclic voltammetry (CV) was measured on a CHI660E electrochemical workstation at a scan rate of 0.1 mV s^{-1} over a potential window of 0.01-3.00 V (vs. Li^+/Li). The charge-discharge characteristics were performed galvanostatically at different current densities between 0.01 and 3.00 V (vs. Li^+/Li) at the temperature of 25 ^{o}C ($\pm$ 1 ^{o}C) by using a LAND-CT2001A test system. The specific capacity and current were calculated based on the mass of NiO (1.24-1.86 mg cm^{-2} for the NiO

nanorod-anchored Ni foam and ~ 0.13 mg cm^{-2} for the directly annealed Ni foam). Electrochemical Impedance Spectroscope (EIS) measurements were conducted with the CHI660E electrochemical workstation in the charged state (3 V vs. Li$^+$/Li). The frequency was from 0.01 Hz to 100 kHz with an excitation voltage of 5 mV.

Results and discussion

The morphology and structure of the prepared NiO nanorod-anchored Ni foam electrode were first studied and presented below. **Figure 1** shows the XRD pattern of the obtained sample, and confirms the formation of NiO phase on the Ni foam substrate. Three weak peaks located at 37.1°, 43.1° and 62.6° well agree with the (111), (200), (220) planes of a face-centered cubic (fcc) NiO (JCPDS 65-2901), respectively. Moreover, three intensive peaks at 44.5°, 51.8° and 76.4° were indexed to the (111), (200) and (220) planes of the fcc Ni foam substrate (JCPDS 65-2865), respectively. The surface microstructure of the NiO nanorod-anchored Ni foam electrode was visualized by SEM with various magnifications (**Figure 2**). Before thermal decomposition, diamond-like nickel oxalate dihydrate blocks with several hundred nanometers in size directly grow on the skeleton surface of nickel foam. And some blocks gather together to form clusters as shown in **Figure S1**. More details were reported in our previous literature.[32] After annealing, it can be seen that NiO nanorods transformed from nickel oxalate dihydrate blocks are uniformly anchored on the skeleton of Ni foam with a three-dimensional network structure (**Figure 2**a, b). The length of the rods is around 1-1.5 μm, and the side length of the quadrilateral

cross section is 200-500 nm. Furthermore, the zoomed-in SEM images (**Figure 2**c, d) show that some clusters are formed by heaping the root-linked rods like blooming flowers. In contrast, **Figure S2** presents the microstructure of the directly annealed Ni foam. NiO nanoparticles with 50-100 nm in size are observed and mainly distributed around the grain boundaries on the skeleton of Ni foam. It is clear that the distribution of these NiO nanoparticles is inhomogeneous, and the mass loading is much less than that of the NiO nanorod-anchored Ni foam electrode.

The morphology and crystal structure of the NiO nanorod-anchored Ni foam electrode were further clarified by TEM observation and electron diffraction (**Figure 3**). **Figure 3**a and b shows bright-field TEM images, clearly displaying the typical rod-like structures. The SAED pattern shown in **Figure 3**c confirms the formation of NiO, and the diffraction rings were indexed to the corresponding ($h\ k\ l$) planes of fcc NiO (JCPDS 65-2901). Here the selected area was $\sim$ 200 nm in diameter, and the SAED results indicate that each rod is composed of NiO nanocrystals. The TEM results are in good agreement with the XRD pattern. **Figure 3**d presents the HRTEM image and corresponding FFT pattern of the NiO nanorod-anchored Ni foam electrode. The rod-like structures are composed of nanocrystals of 10-15 nm in size. The spacing of some lattice fringes is 2.45 Å, which is close to that (2.42 Å) of the (111) crystal plane of NiO. The corresponding FFT pattern (inset of **Figure 3**d) further verifies the nanocrystalline nature of the NiO nanorods.

The BET surface area and porous characteristics of the NiO nanorod-anchored Ni foam electrode were determined by N_2 adsorption-desorption measurements. The N_2

adsorption-desorption isotherms of the samples (**Figure 4**a) correspond well to the type IV curve with a hysteresis loop, indicating the presence of mesoporosity. According to the adsorption-desorption isotherms, the BET surface area of the NiO nanorod-anchored Ni foam was calculated to be 3.70 m^2 g^{-1} (normalized by the total mass of the electrode). When we just take the active material (NiO) into consideration, the specific surface area reaches as high as 68.29 m^2 g^{-1}. **Figure 4**b displays pore size distribution measured from the adsorption branch of isotherm using the BJH method. The average pore diameter of the samples is in the mesoporous region, with multimodal pore size distributions. The pore size distribution mainly centers in the range of 2-10 nm. Some nanopores could be discerned in TEM images, as highlighted by dotted arrows in **Figure 3b**. And the total pore volume of pores with the diameter of 1.964-334.773 nm is 0.315 cm^3 g^{-1}. It is believed that the high specific surface area and porous structures of the NiO anchored Ni foam electrode would facilitate the diffusion of ions, improving the electrochemical performance.

Electrochemical tests including cyclic voltammetry and galvanostatic discharge/charge cycling were conducted to evaluate the performance of the NiO nanorod-anchored Ni foam electrode. As shown in **Figure 5**a, the CV profiles of the NiO electrode are similar except for the first scan. A strong cathodic peak located around 0.37 V (vs. Li^+/Li) can be observed in the first cycle, which is attributed to the initial reduction of NiO to Ni and the formation of amorphous Li_2O (NiO + $2Li^+$ + $2e^-$ → Ni + Li_2O) and a partially reversible solid electrolyte interface (SEI) layer.[8,33] Smaller anodic peak at round 1.45 V (vs. Li^+/Li) corresponds to the partial

decomposition of the polymeric coating on the NiO surface, while the conversion of Ni to NiO and the decomposition of Li_2O to Li^+ ($Ni + Li_2O \rightarrow NiO + 2Li^+ + 2e^-$) account for another anodic peak at 2.25 V (vs. Li^+/Li), **Figure 5**a. The reduction peaks shift to about 1.01 V (vs. Li^+/Li) with a shoulder around 1.40 V (vs. Li^+/Li) for the subsequent cycles, suggesting the dramatic lithium driven, structural or textural modifications during the first lithiation process (**Figure 5**a).[23,33] The peak intensity and integral areas are similar from the second to the fifth cycle, showing good cycling stability. **Figure 5**b presents the potential versus capacity profiles in the 1st, 2nd, 10th, 35th and 70th cycles at 1 A g^{-1}. The open circuit voltage (OCV) of the fabricated cells is 3.09 V (vs. Li^+/Li). The potential decreases rapidly in the first discharge, followed by an extended plateau around 0.73 V (vs. Li^+/Li), corresponding to the reduction of NiO and the formation of SEI layer. In the following discharge cycles, the voltage plateaus at about 1.05 V (vs. Li^+/Li) appear higher and more sloping with a lower overpotential than that in the first discharge, indicating that the Li^+ insertion in the successive cycles is easier (**Figure 5**b). The charge plateaus located at about 1.45 V and 2.25 V (vs. Li^+/Li) represent the partial decomposition of the SEI film and the reverse reaction for the formation of NiO, respectively (**Figure 5**b).[33,34] From the second cycle, the electrode maintains high reversibility. These results have a good agreement with the CV measurement (**Figure 5**a).

Figure 6 displays an excellent cycling stability and high coulombic efficiency of the NiO nanorod-anchored Ni foam electrode at high current densities of 1 A g^{-1} (**Figure 6**a) and 2 A g^{-1} (**Figure 6**b). **Table 1** summarizes the corresponding results

originating from **Figure 6**. The first discharge/charge capacity is 1126.7/802.4 mAh g^{-1} and 1093.3/753.7 mAh g^{-1}, with high initial coulombic efficiency of 71.2% and 68.9% for 1 A g^{-1} and 2 A g^{-1}, respectively (**Table 1**). The irreversible capacity during the first cycle is mainly attributed to the formation of SEI layer and incomplete decomposition of Li$_2$O phase, as well as other factors such as intrinsic nature of the material and kinetic limitations (due to current densities).[35,36] Furthermore, the reversible capacity after the 2nd and 70th cycles is 742.1 mAh g^{-1} and 705.5 mAh g^{-1} respectively, exhibiting only 4.9% capacity fade at 1 A g^{-1}. Even at a higher current density of 2 A g^{-1}, the charge capacity still remains at 548.1 mAh g^{-1} at the end of the 70th cycle. Besides, the insets of **Figure 6** clearly show that the coulombic efficiency is ≥ 98% in the range of 2nd-70th cycles at both high current densities. This performance of the NiO nanorod-anchored Ni foam electrode is much better than the directly annealed Ni foam electrode (**Figure S3**) and most of the previous reports as presented in **Table 2**.[10,12,13,15,16,21,24,27,37,38] The directly annealed Ni foam electrode delivered the first discharge/charge capacity of 1336.1/743.5 mAh g^{-1} with low initial coulombic efficiency of 55.6% at 2 A g^{-1}. During the cycling process, the directly annealed Ni foam electrode showed drastic degradation with a charge capacity of 302.6 mAh g^{-1} after 70 cycles (**Figure S3**). In **Table 2**, NiO/CMK-3 electrodes fabricated by hydrophobic encapsulation ran only 50 cycles with relatively low (88.2%) retention at 1000 mA g^{-1}.[37] Besides, NiO nanofibers by electrospinning technique and heat treatment delivered much lower reversible capacity of 583 mAh g^{-1} at an extremely low current density of 80 mA g^{-1}.[12] The longer cycling stability

and higher rate performance of the NiO nanorod-anchored Ni foam electrode might be ascribed to the NiO nanorods grown directly on Ni foam free of any binder/additive. This unique structure could form a better adhesion and excellent electrical contact between NiO and the current collector of Ni foam, improving the reaction kinetics of NiO anode, especially at high current densities.[27] At the same time, the three-dimensional porous architecture of Ni foam and the NiO nanorod arrays on the framework can provide short diffusion paths for lithium ions and allow efficient ingress and infiltration of the electrolyte into the electrode.[39,40] Additionally, the high specific surface area and nanocrystalline nature of the NiO nanorods also account for the high performance of the present electrodes.

The rate performance of the NiO nanorod-anchored Ni foam electrode at various current densities is shown in **Figure 7**. With increasing current densities, the separations between the discharge plateaus and charge plateaus are enlarged due to the dynamic limitation, rendering higher overpotential (**Figure 7**a).[30,41] **Figure 7**b shows the rate capability of the electrode. After every 10 cycles at specific current densities, the reversible capacities are about 936, 879, 804, 715, 575 mAh g^{-1}, decreasing regularly with increasing current densities of 0.2, 0.5, 1, 2, 5 A g^{-1} with coulombic efficiency of $\geq$ 99%. More importantly, when the current density is returned to 0.5 A g^{-1}, the electrode could recover its capacity to about 945 mAh g^{-1}, indicating that the NiO nanorod-anchored Ni foam electrode has good structural stability and rate performance. It is noteworthy that, the slightly higher reversible capacity may be ascribed to the reversible growth of a polymeric gel-like film resulting from

kinetically activated electrolyte degradation and the pseudocapacitive properties of NiO.[42-45] Similar phenomena were frequently observed in conversion reaction-based anode materials, such as Co_3O_4,[46-49] MnO/graphene,[50] and also other NiO nanostructures and hybrids.[17-20]

As seen in **Figure 8**, EIS measurements of the NiO nanorod-anchored Ni foam electrode were conducted in the charged state (3 V vs. Li^+/Li) after the 10th, 30th, 50th, 70th and 80th cycles. And the data of the Nyquist plots were analyzed by fitting to a simple equivalent circuit (**Figure 8**b). Among the electrical elements, R_e represents the resistance of electrolyte. R_{sei} is the SEI film resistance and C_{sei} is the corresponding capacitance. R_{ct} is defined as the lithium ion charge transfer resistance while C_{dl} is the double-layer capacitance. Z_w and C_{int} mean the Warburg diffusion impedance and the intercalation capacitance, respectively (**Figure 8**b). The resistance values obtained from the impedance spectra are summarized in **Table 3**. Much sharper slope of the straight beelines at low frequency are observed after the 30th-80th cycles than the one after the 10th cycle according to the Nyquist plots (**Figure 8**a) which is attributed to the rougher surface of NiO nanorod arrays during the first ten charge-discharge cycles, leading to larger interface between active materials and the electrolyte. Additionally, the similar intercept of R_e at the real axis in the high frequency region and the values of R_{ct} at medium frequency imply that the NiO nanorod-anchored Ni foam electrode possesses low and stable electrolyte resistance and almost constant lithium ion charge transfer resistance, respectively (**Table 3**).[14,38] Moreover, the values of R_{sei} at high frequency are nearly constant after the 10th cycle,

suggesting a stable formation of SEI layer. To further confirm the structural integrity of the NiO nanorod-anchored Ni foam electrode, we also observed the microstructure of the NiO nanorod-anchored Ni foam electrode after 70 charge/discharge cycles between 0.01-3 V (vs. Li^+/Li) at 1 A g^{-1} (**Figure S4). Figure S4**a presents that the relatively rough skeleton surface of the Ni foam is covered with a smooth SEI layer, which was formed during the first lithiation process.[8,28] Apparently, several inter-cracks can be observed due to the fast volume expansion and shrink for 70 times (**Figure S4**a). However, the rod-like structures still remain across a large area as presented in **Figure S4**b, indicating that the 3D porous Ni foam supported NiO nanorod arrays are stable and can be sustained during cycling. It is obvious that the special morphology can maintain structural integrity by accommodating partially the strain induced by the volume change during the fast charge/discharge process.[19,51] Additionally, NiO nanorods grown directly on Ni foam could enhance the electrical conductivity. In order to quantify the conductivity of the NiO nanorod-anchored Ni foam electrode, the resistance of pure Ni foam and NiO anchored Ni foam electrode was measured by the four-electrode method. And the calculated resistivity of the NiO anchored Ni foam was 2.95 μΩ•m, which is only 1.3 times that (2.33 μΩ•m) of the pure Ni foam, further demonstrating the excellent conductivity of the electrode.

Conclusions

In summary, the NiO nanorod-anchored Ni foam could be prepared by the facial anodization route combined with annealing treatment. The morphological and

structural characterization reveals that the uniform NiO nanorod arrays directly grow on the skeleton surface of Ni foam, and some NiO nanorods form blooming flower-like clusters. When being applied as anode materials free of any binder/additive in lithium-ion batteries, the NiO nanorod-anchored Ni foam electrode delivers a high reversible lithium storage capacity of around 705.5 mAh g^{-1} and 548.1 mAh g^{-1} after 70 cycles with high coulombic efficiency at 1 and 2 A g^{-1}, respectively. Moreover, the electrode exhibits excellent rate capability and can resume its original capacity of about 945 mAh g^{-1} at the relatively low current density. We believe that the binder-free NiO nanorod-anchored Ni foam electrode could be a promising candidate for high capacity, economical and environmentally friendly anode for high power LIBs. And the rapid and economical anodization/annealing strategy can be exploited to fabricate other transition metal oxide nanostructures, presumably offering excellent electrochemical properties.

Acknowledgements

References

1   M. Armand and J.-M. Tarascon, *Nature*, 2008, **451**, 652.

2   B. Kang and G. Ceder, *Nature*, 2009, **458**, 190.

3   J. B. Goodenough and Y. Kim, *Chem. Mater.* , 2009, **22**, 587.

4   V. Etacheri, R. Marom, R. Elazari, G. Salitra and D. Aurbach, *Energy Environ. Sci.* , 2011, **4**, 3243.

5   J.-M. Tarascon and M. Armand, *Nature*, 2001, **414**, 359.

6   Y. Su, S. Li, D. Wu, F. Zhang, H. Liang, P. Gao, C. Cheng and X. Feng, *ACS Nano*, 2012, **6**, 8349.

7   A. S. Aricò, P. Bruce, B. Scrosati, J.-M. Tarascon and W. Van Schalkwijk, *Nat. Mater.* , 2005, **4**, 366.

8   P. Poizot, S. Laruelle, S. Grugeon, L. Dupont and J. Tarascon, *Nature*, 2000, **407**, 496.

9   J. Cabana, L. Monconduit, D. Larcher and M. R. Palacin, *Adv. Mater.* , 2010, **22**, E170.

10   X. Li, A. Dhanabalan and C. Wang, *J. Power Sources*, 2011, **196**, 9625.

11   S. A. Needham, G. Wang and H. K. Liu, *J. Power Sources* 2006, **159**, 254.

12   V. Aravindan, P. Suresh Kumar, J. Sundaramurthy, W. C. Ling, S. Ramakrishna and S. Madhavi, *J. Power Sources*, 2013, **227**, 284.

13   Y. Mai, J. Tu, X. Xia, C. Gu and X. Wang, *J. Power Sources*, 2011, **196**, 6388.

14   H. Liu, G. Wang, J. Liu, S. Qiao and H. Ahn, *J. Mater. Chem.* , 2011, **21**, 3046.

15   Y. Yuan, X. Xia, J. Wu, J. Yang, Y. Chen and S. Guo, *Electrochem. Commun.*,

2010, **12**, 890.

16   B. Wang, J. Cheng, Y. Wu, D. Wang and D. He, *Electrochem. Commun.*, 2012, **23**, 5.

17   X. Wang, L. Qiao, X. Sun, X. Li, D. Hu, Q. Zhang and D. He, *J. Mater. Chem. A*, 2013, **1**, 4173.

18   W. Wen, J.-M. Wu and M.-H. Cao, *Nano Energy*, 2013, **2**, 1383.

19   X. Wang, X. Li, X. Sun, F. Li, Q. Liu, Q. Wang and D. He, *J. Mater. Chem.*, 2011, **21**, 3571.

20   X. Wang, Z. Yang, X. Sun, X. Li, D. Wang, P. Wang and D. He, *J. Mater. Chem.*, 2011, **21**, 9988.

21   Y. Zou and Y. Wang, *Nanoscale*, 2011, **3**, 2615.

22   G. Zhou, D.-W. Wang, L.-C. Yin, N. Li, F. Li and H.-M. Cheng, *ACS Nano*, 2012, **6**, 3214.

23   Y. Xia, W. Zhang, Z. Xiao, H. Huang, H. Zeng, X. Chen, F. Chen, Y. Gan and X. Tao, *J. Mater. Chem.*, 2012, **22**, 9209.

24   W. Wen, J.-M. Wu and M.-H. Cao, *J. Mater. Chem. A*, 2013, **1**, 3881.

25   C. Wang, D. Wang, Q. Wang and H. Chen, *J. Power Sources* 2010, **195**, 7432.

26   X. Huang, J. Tu, X. Xia, X. Wang and J. Xiang, *Electrochem. Commun.*, 2008, **10**, 1288.

27   X. Li, A. Dhanabalan, K. Bechtold and C. Wang, *Electrochem. Commun.*, 2010, **12**, 1222.

28   R. A. Susantyoko, X. Wang, Q. Xiao, E. Fitzgerald and Q. Zhang, *Carbon*,

2014, **68**, 619.

29   I. Kovalenko, B. Zdyrko, A. Magasinski, B. Hertzberg, Z. Milicev, R. Burtovyy, I. Luzinov and G. Yushin, *Science*, 2011, **334**, 75.

30   B. Varghese, M. Reddy, Z. Yanwu, C. S. Lit, T. C. Hoong, G. Subba Rao, B. Chowdari, A. T. S. Wee, C. T. Lim and C.-H. Sow, *Chem. Mater.*, 2008, **20**, 3360.

31   X.-Y. Xue, S. Yuan, L.-L. Xing, Z.-H. Chen, B. He and Y.-J. Chen, *Chem. Commun.*, 2011, **47**, 4718.

32   G. Cheng, J. Xu, C. Dong, W. Yang, T. Kou and Z. Zhang, *J. Mater. Chem. A*, 2014, **2**, 17307.

33   S. Grugeon, S. Laruelle, R. Herrera-Urbina, L. Dupont, P. Poizot and J. Tarascon, *J. Electrochem. Soc. *, 2001, **148**, A285.

34   X. Liu, S. W. Or, C. Jin, Y. Lv, C. Feng and Y. Sun, *Carbon*, 2013, **60**, 215.

35   M. Reddy, T. Yu, C.-H. Sow, Z. X. Shen, C. T. Lim, G. Subba Rao and B. Chowdari, *Adv. Funct. Mater. *, 2007, **17**, 2792.

36   D. Su, M. Ford and G. Wang, *Sci. Rep.*, 2012, **2**.924

37   M.-Y. Cheng and B.-J. Hwang, *J. Power Sources*, 2010, **195**, 4977.

38   G.-P. Kim, S. Park, I. Nam, J. Park and J. Yi, *J. Power Sources*, 2013, **237**, 172.

39   P.-L. Taberna, S. Mitra, P. Poizot, P. Simon and J.-M. Tarascon, *Nat. Mater.*, 2006, **5**, 567.

40   C. Ban, Z. Wu, D. T. Gillaspie, L. Chen, Y. Yan, J. L. Blackburn and A. C.

Dillon, *Adv. Mater.*, 2010, **22**, E145.

41   H.-W. Lee, P. Muralidharan, R. Ruffo, C. M. Mari, Y. Cui and D. K. Kim, *Nano Lett.* , 2010, **10**, 3852.

42   S. Grugeon, S. Laruelle, L. Dupont and J.-M. Tarascon, *Solid State Sci.* , 2003, **5**, 895.

43   G. Zhou, D.-W. Wang, F. Li, L. Zhang, N. Li, Z.-S. Wu, L. Wen, G. Q. Lu and H.-M. Cheng, *Chem. Mater.* , 2010, **22**, 5306.

44   J. Y. Shin, D. Samuelis and J. Maier, *Adv. Funct. Mater.* , 2011, **21**, 3464.

45   C. T. Cherian, J. Sundaramurthy, M. Kalaivani, P. Ragupathy, P. S. Kumar, V. Thavasi, M. Reddy, C. H. Sow, S. G. Mhaisalkar and S. Ramakrishna, *J. Mater. Chem.* , 2012, **22**, 12198.

46   L. Li, K. H. Seng, Z. Chen, Z. Guo and H. K. Liu, *Nanoscale*, 2013, **5**, 1922.

47   J. Wang, N. Yang, H. Tang, Z. Dong, Q. Jin, M. Yang, D. Kisailus, H. Zhao, Z. Tang and D. Wang, *Angew. Chem.*, 2013, **125**, 6545.

48   N. Du, H. Zhang, B. Chen, J. Wu, X. Ma, Z. Liu, Y. Zhang, D. Yang, X. Huang and J. Tu, *Adv. Mater.* , 2007, **19**, 4505.

49   X. Wang, Y. Fan, R. Agung Susantyoko, Q. Xiao, L. Sun, D. He and Q. Zhang, *Nano Energy*, 2014, **5**, 91.

50   Y. Sun, X. Hu, W. Luo, F. Xia and Y. Huang, *Adv. Funct. Mater.* , 2013, **23**, 2436.

51   X. Jia, Z. Chen, A. Suwarnasarn, L. Rice, X. Wang, H. Sohn, Q. Zhang, B. M. Wu, F. Wei and Y. Lu, *Energy Environ. Sci.* , 2012, **5**, 6845.

Table 1. The lithium storage performance of the NiO nanorod-anchored Ni foam electrode (corresponding to **Figure 6**).

Current densities ($A\,g^{-1}$)	1st discharge / charge capacity ($mA\,h\,g^{-1}$)	Initial coulombic efficiency	Coulombic efficiency (2nd-70th cycle)	2nd reversible capacity ($mA\,h\,g^{-1}$)	70th reversible capacity ($mA\,h\,g^{-1}$)	Fading rate (2nd-70th cycle)
1	1126.7 / 802.4	71.2%	≥ 98%	742.1	705.5	~ 4.9%
2	1093.3 / 753.7	68.9%	≥ 98%	682.8	548.1	~ 19.7%

Table 2. The lithium storage performance of NiO or the composite electrodes in recent 4 years.

Materials	Method	Current density (mA g^{-1})	Cyclability / Retention rate	Reversible Capacity (mAh g^{-1})	Ref.
NiO	anodization	1000	70 / 95.1%	705.5	our work
		2000	70 / 80.3%	548.1	
NiO / CMK-3	hydrophobic encapsulation	1000	50 / 88.2%	716	37
NiO	electrodeposition	718	50 / 72%	518	15
NiO / C	agarose-mediated electrodeposition	718	100 / 78%	604	38
NiO / Ni	precipitation	360	40 / 84.3%	~610	24
NiO-Ni	electrostatic spray deposition	286	100 / 95.1%	~370	10
Ni / NiO	gas-solid oxidation	156	65 / 92.2%	646	27
Co-doped NiO	chemical bath deposition	100	50 / 66.8%	589.5	13
NiO	electrospinning	80	100 / 75%	583	12
NiO-GNS	hydrothermal reaction	71.8	40 / 97.6%	1031	21
NiO	electrospinning	40	50 / 91.4%	638	16

Table 3. Fitting results obtained from the EIS data in **Figure 8**.

| State	R_e (Ω)	R_{sei} (Ω)	R_{ct} (Ω)
After the 10th cycle	6.66	2.46	12.03
After the 30th cycle	6.37	5.93	11.41
After the 50th cycle	6.39	4.19	9.81
After the 70th cycle	6.15	4.43	10.91
After the 80th cycle	6.28	4.90	12.25
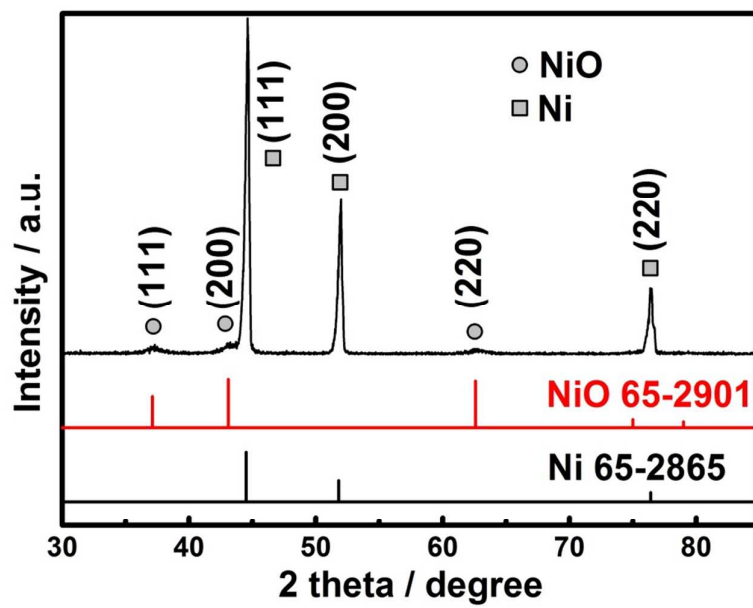
Figure 1. XRD pattern of the NiO nanorod-anchored Ni foam electrode.
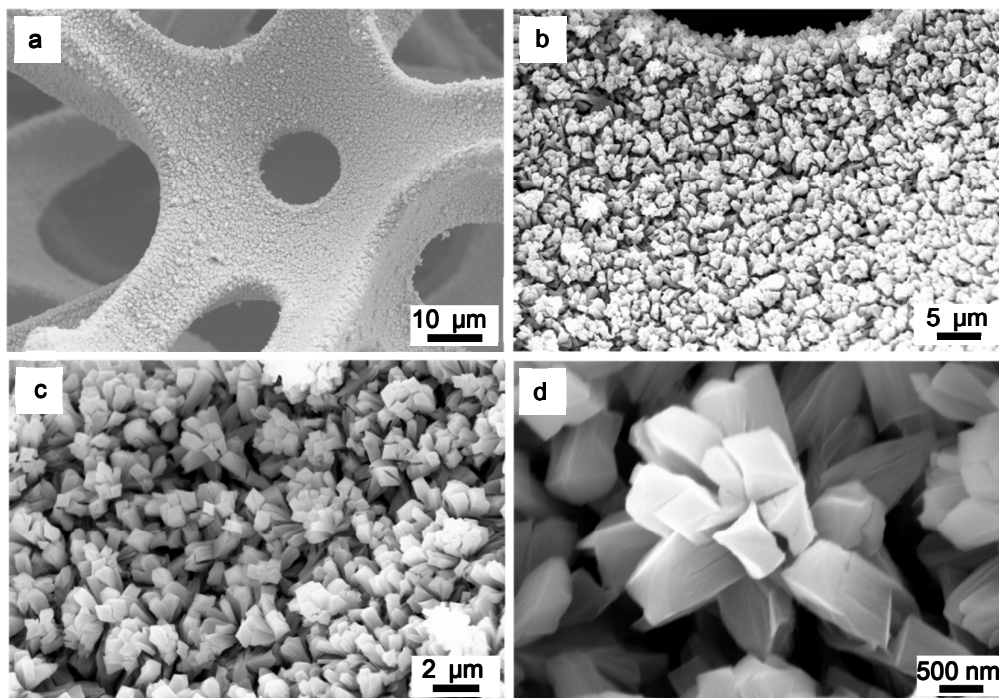
**Figure 2**. SEM images of the NiO nanorod-anchored Ni foam electrode.
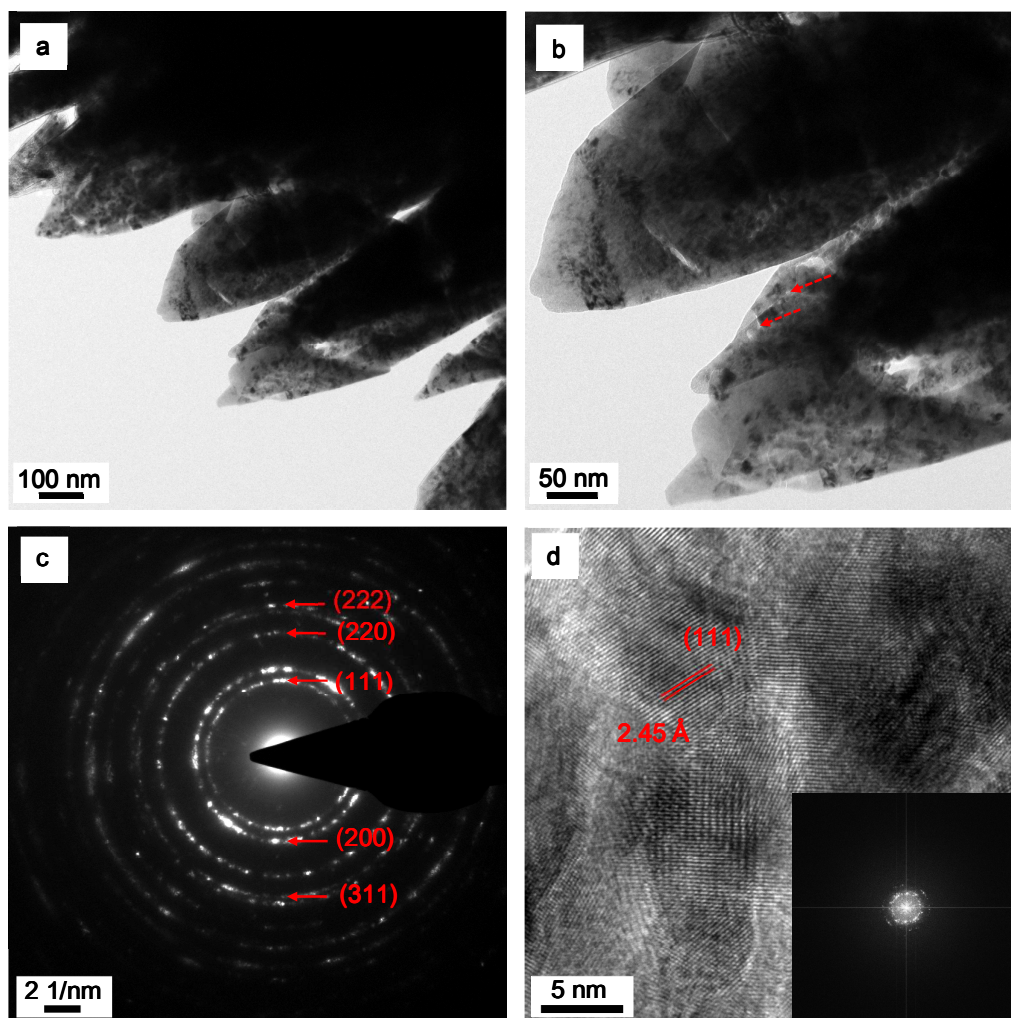
Figure 3. (a, b) TEM images, (c) SAED pattern and (d) HRTEM image of the NiO

nanorod-anchored Ni foam electrode. Inset of (d) shows the FFT pattern

corresponding to the HRTEM image.
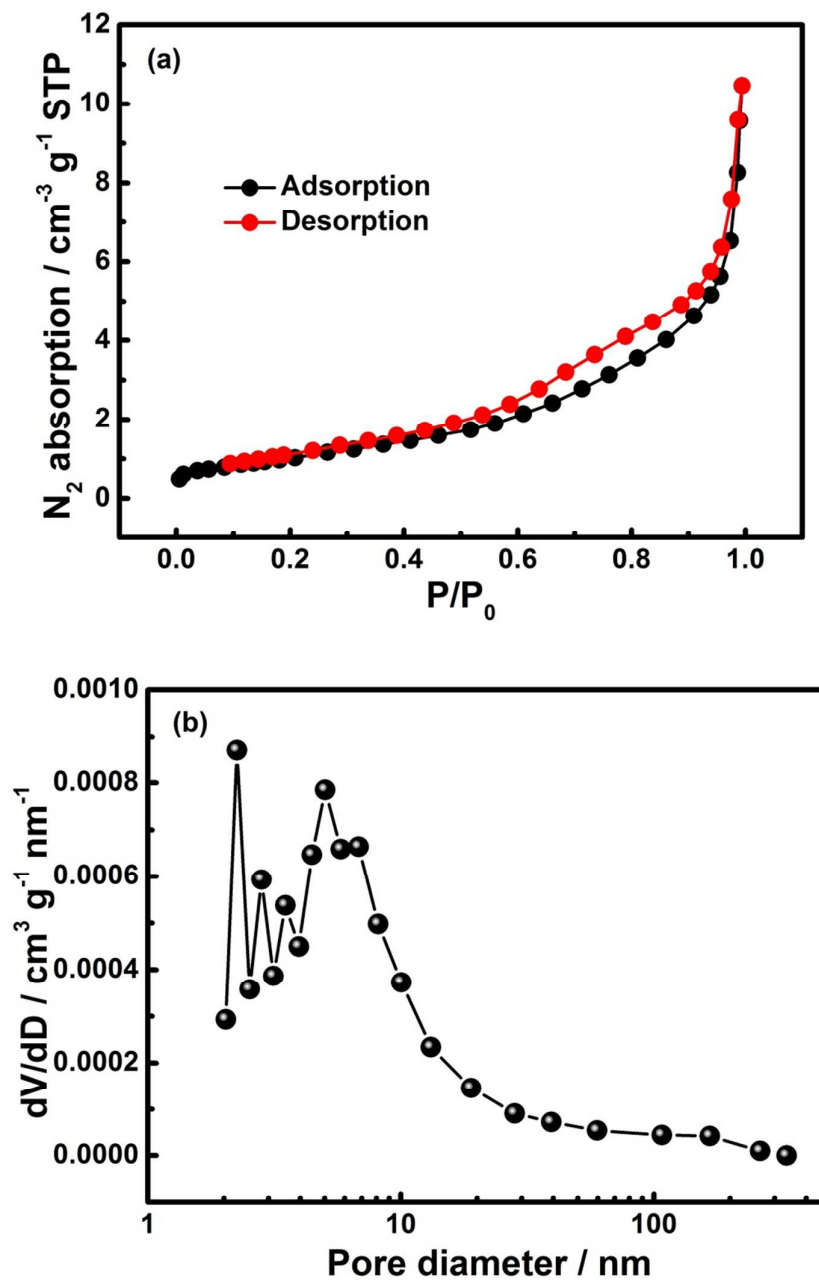
Figure 4. (a) N_2 adsorption-desorption isotherms and (b) pore size distribution of the

NiO nanorod-anchored Ni foam electrode (based on the total mass of the electrodes).
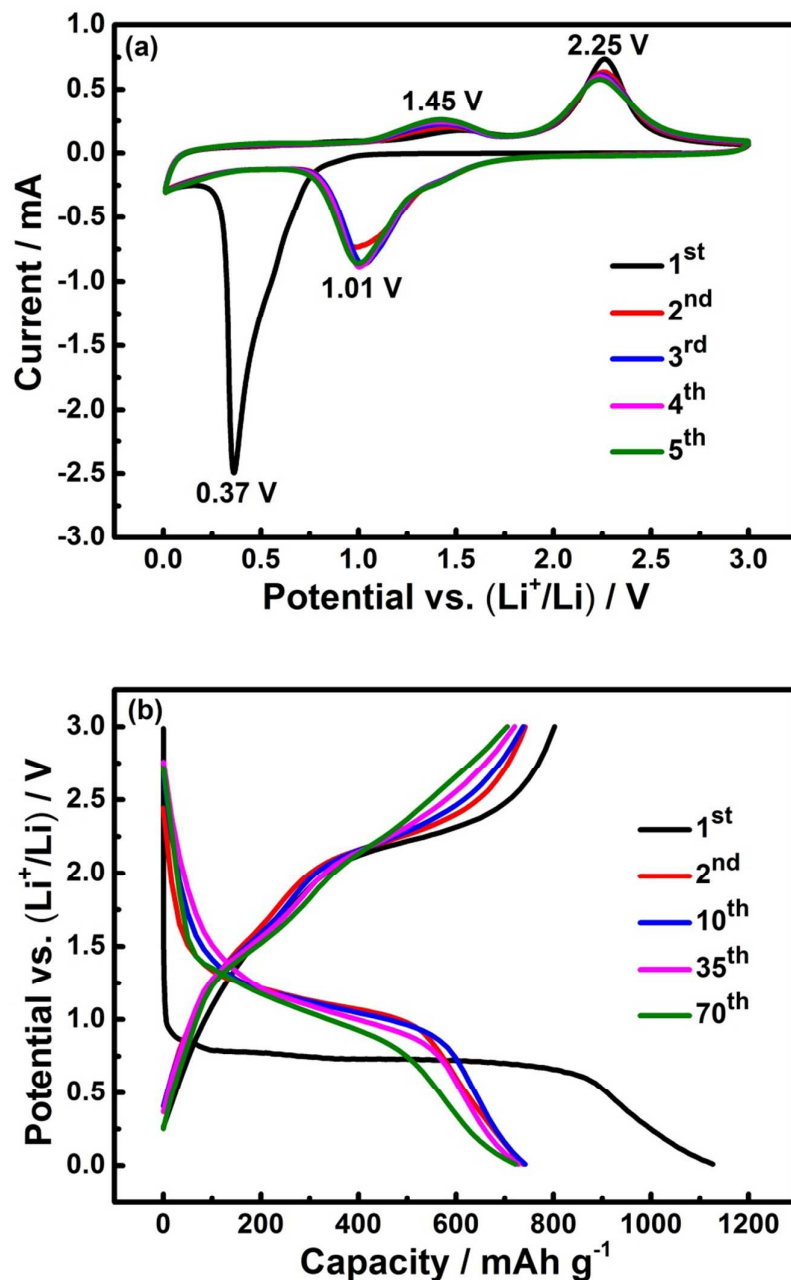
Figure 5. (a) Cyclic voltammograms of the NiO nanorod-anchored Ni foam electrode over a potential window of 0.01-3 V (vs. Li$^+$/Li) at a scan rate of 0.1 mV s^{-1}. (b) Galvanostatic charge-discharge curves of the NiO nanorod-anchored Ni foam at different cycles in a potential range of 0.01-3 V (vs. Li$^+$/Li) at a current density of 1 A g^{-1}.
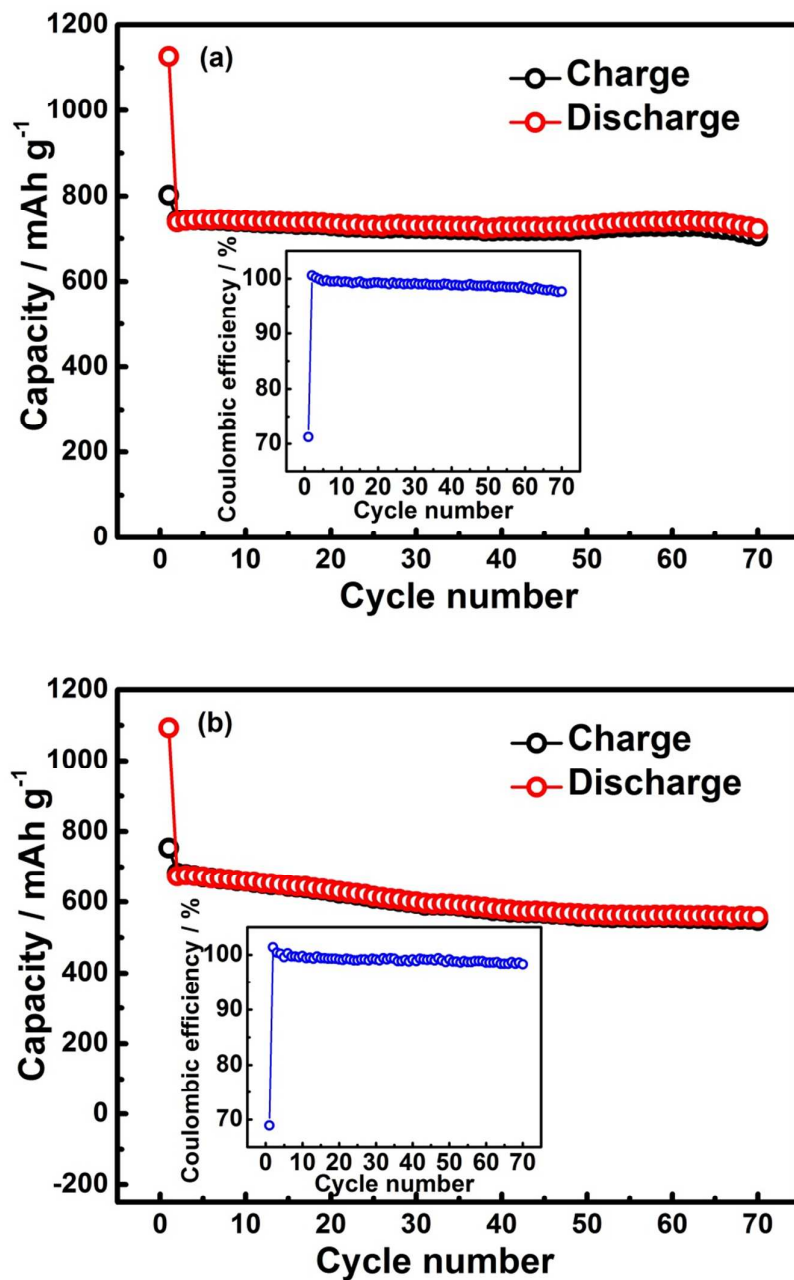
Figure 6. Cycling performance of the NiO nanorod-anchored Ni foam electrode at a current density of (a) 1 A g^{-1} and (b) 2 A g^{-1}. Insets of (a, b) show the corresponding coulombic efficiency.
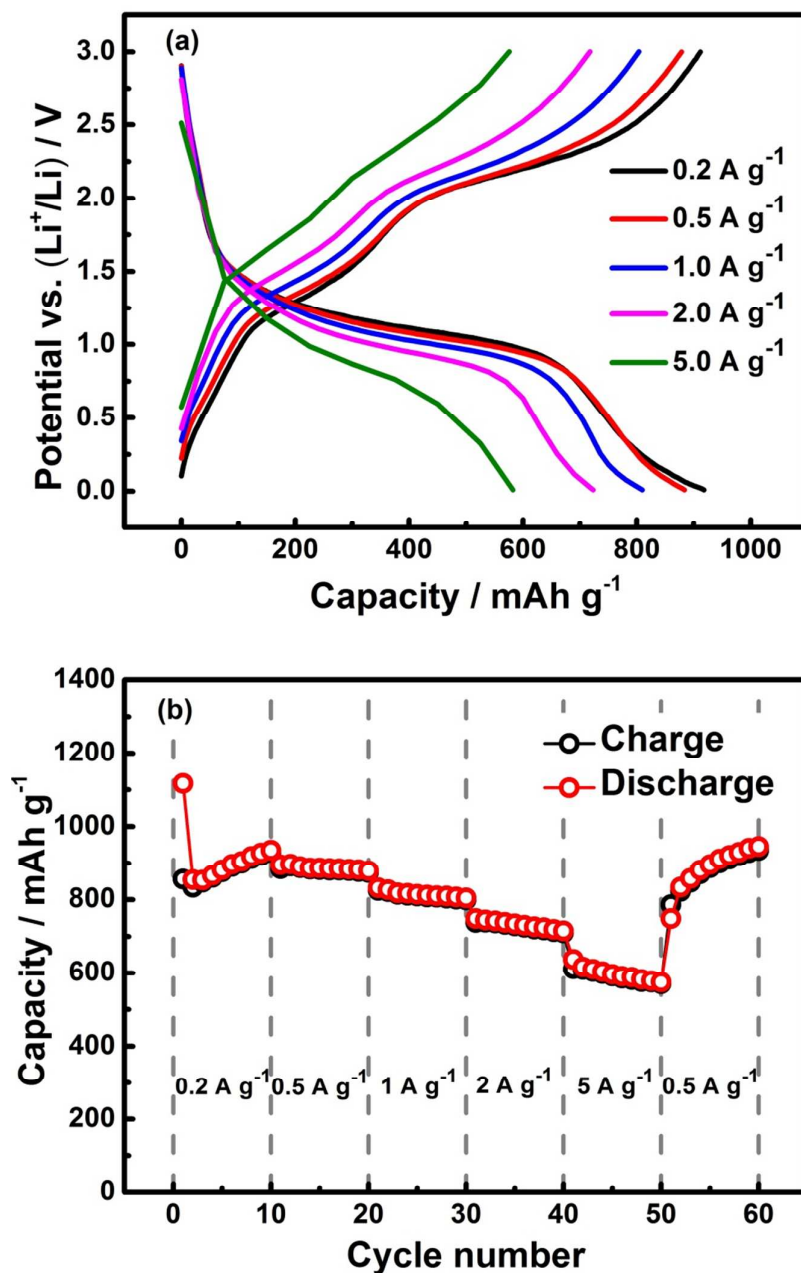
Figure 7. (a) Representative charge-discharge profiles of the NiO nanorod-anchored

Ni foam electrode at varied current densities. (b) Rate performance of the NiO

nanorod-anchored Ni foam electrode at varied current densities.
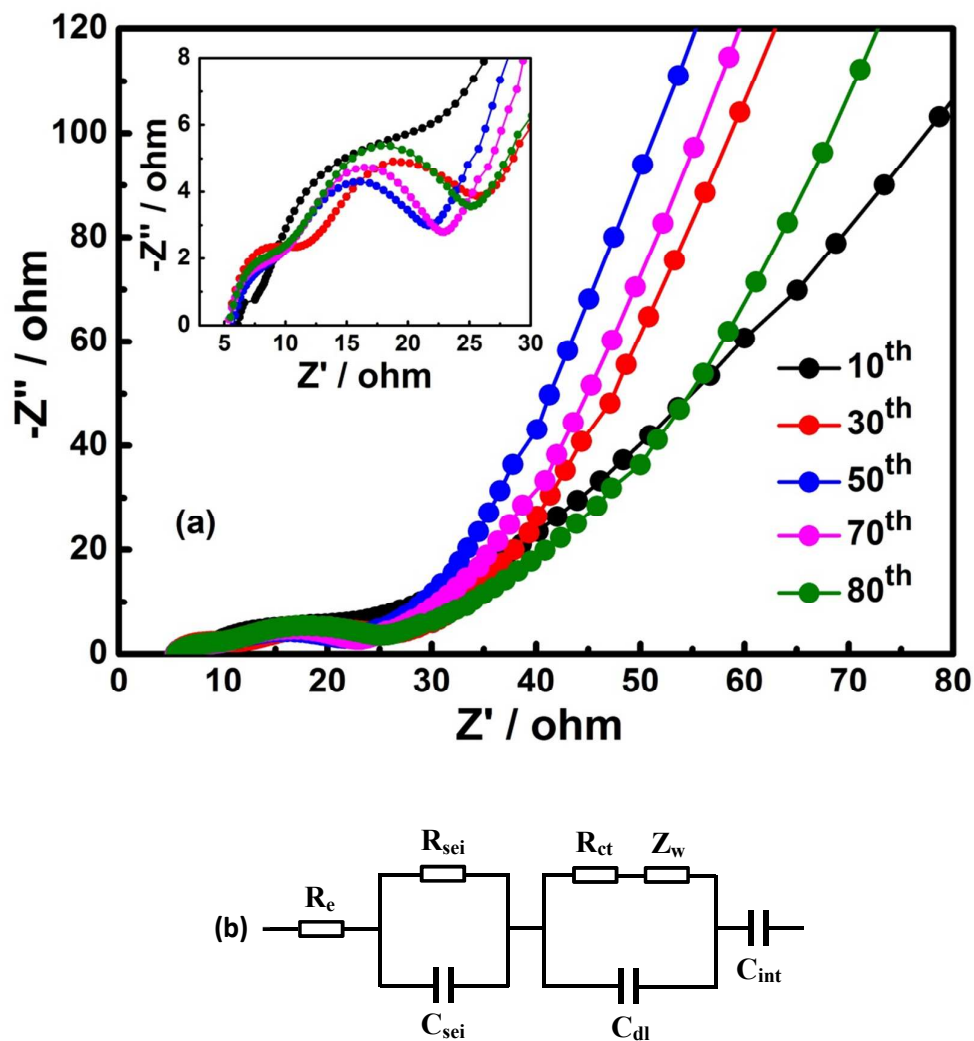
Figure 8. (a) Nyquist plots of the NiO nanorod-anchored Ni foam electrode after different cycles at a current density of 1 A g^{-1} in the charged state (3 V vs. Li^{+}/Li) over the frequency range of 0.01 Hz-100 kHz. Inset of (a) shows the enlarged parts at high frequency region. (b) Equivalent electrical circuit corresponding to the Nyquist plots.

Table of Contents
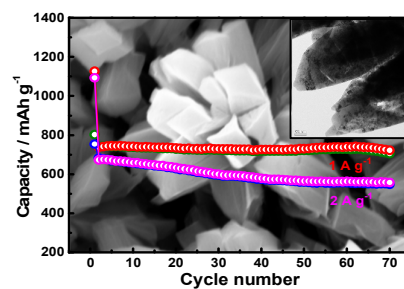
3D binder-free NiO nanorod-anchored Ni foam electrodes synthesized by in-situ anodization and annealing exhibit superior cyclability and high rate performance.